A rapid numerical method to constrain 2D focused fluid flow rates along convergent margins using dense BSR-based temperature field data

Pascal Kunath*[1, 2], Wu-Cheng Chi[2], Christian Berndt[3] , and Char-Shine Liu[4]

[1] Institute of Oceanography, National Taiwan University, Taiwan

[2]Institute of Earth Sciences, Academia Sinica, Taiwan

[3]Helmholtz Centre for Ocean Research Kiel, GEOMAR, Germany

[4]Ocean Center, National Taiwan University, Taiwan

Abstract

Estimates of the sub-seabed fluid flow rates are important for understanding hydrological budgets, biogeochemical cycles, and physical properties of the sediments. Fluid flow rates and directions, however, are difficult to measure, particularly beneath the seafloor. We developed a rapid method to estimate regional fluid migration rates using an extensive database of seismic reflection profiles taken offshore SW Taiwan. We observe bottom-simulating reflector (BSR) that deflect towards the seafloor near thrust faults that indicate localized heat flow variations. At these sites, advecting warm pore fluids transport heat to shallower depths and force the BSR shallower. Our 2-D steady-state numerical method quantifies the fluid flow rates required to cause such thermal anomalies. We found that fluid flow rates near the trench of the accretionary wedge range between 0.1 to 16 m^3 yr^{-1} m^{-1}, with slower and faster rates generally associated with slope basin discontinuities and faults, respectively. To evaluate the fluid pattern evolution from subduction to collision, we studied three transects: one along the Manila subduction zone in the south and two in Taiwan's initial collision zone in the north. We quantified the fluid budget and partitioning of fluid flow between focused discharge through faults and diffusive flow through the wedge. Faults in Taiwan's accretionary wedge capture on average 25% of the total dewatering flux in the younger subduction zone and 38.5% in the tectonically mature collision zone. Our method provides estimates of fluid migration rates along convergent plate boundaries, and contributes to our understanding of focused fluid flow processes in many other regions.

Plain Language Summary

Fluids play a key role for many subduction zone processes. However, quantitative constraints on flow expulsion rates and directions are limited. Efficient upward fluid migration through subbottom conduits can be generated tectonically, such as faults. Faults are ubiquitous along convergent margins; yet, a quantitative understanding of their impact on regional fluid budgets, flow rates and distribution at vent sites remains unclear. We developed a rapid numerical method to constrain 2D focused fluid flow rates using seismically derived thermal structure and applied it to the subduction-collision zone system off SW Taiwan. To study the influence of long-term tectonic processes on the fluid budget, we remotely mapped the distribution and amount of focused fluid flow across the convergent margin, using a widespread shallow subbottom temperature field derived from a spatially-dense seismic dataset covering an area of more than 25000 km^2. We combined the results with other previous published geophysical datasets to calculate the margin fluid budget. We found stronger fluid advection from depth along the collision zone, where thicker sediments are deformed more intensively. Our approach to quantify fluid fluxes is applicable to a range of tectonic regimes and can provide critical insight into local, regional, or even global fluid budget estimates.

Keywords:

marine seismic, gas hydrate, Taiwan, thermal modeling, fluid migration rates, fluid budget

Key Points:

- Developed a method to quantify fluid flow rates from BSR-based temperature data.
- Identified fluid partitioning patterns off SW Taiwan from subduction to collision.
- Focused fault-related flow controls the local depth of the hydrate stability zone.

1. Introduction

Fluid flow in the shallow sediments along continental margins has considerable implications for regional seismological and tectonic processes. Specifically, the dewatering of the accretionary wedge between convergent plates affects the thermal transfer, pore water geochemistry, gas and oil reservoir formation, seismogenic processes, and the mechanical behavior of the crust (e.g. Saffer & Tobin, 2011; and references therein). Flow rates and directions, however, are difficult to quantify beneath the seafloor, without significant investment in infrastructure and time.

Fluid flow through the earth’s crust may occur diffusively through the rock matrix at relatively low rates across the entire wedge or along focused, localized conduits, including fractures, faults and mud volcanoes at relatively faster rates (Carson & Screaton, 1998; Hensen et al., 2004; Lauer & Saffer, 2012; Ranero et al., 2008). Fluid migration rates are typically measured in-situ in boreholes or using seafloor-monitoring systems (e.g. Carson et al., 1991; Screaton et al., 1995; Davis & Villinger, 2006); although some studies use borehole temperature or thermal probe data to study flow rates, where temperature acts as a tracer. It is difficult, however, to derive a systematic, quantitative understanding of the fluid budget, flow rates, and distribution at vent sites using localized measurements. In this case, the primary limitation is uncertainty regarding the applicability of extending borehole measurements laterally to regions tens of kilometers away. In addition, densely sampled in-situ temperature measurements are expensive and scarce. As such, a remote sensing method to derive temperature field and regional fluid flow patterns in the shallow marine sediments would be advantageous in overcoming these limitations.

The common occurrence of gas hydrate, an ice-like compound of natural gas and water, along continental margins provides a unique opportunity to derive dense temperature field information under the seabed from seismic data. Hydrate is stable at high pressures and low temperatures, which makes its formation favorable along most continental margins. As the temperature increases with depth, however, hydrate eventually becomes unstable at a distinct, predictable depth beneath the seafloor, defined as the base of the gas hydrate stability zone (BGHSZ). The BGHSZ is typically identified in seismic data from the presence of a strong, bottom-simulating reflector (BSR; Shipley, 1979). The BSR occurs in response to the acoustic impedance contrast between overlying hydrate-bearing and underlying gas-bearing sediments. Since the hydrate phase boundary is well constrained, an estimate of the temperature at the BSR can be derived from the hydrostatic pressure at the BSR, assuming no overpressure, and the hydrate stability curve at seawater salinity. With the BSR temperature constrained, the regional and local geothermal gradients and heat fluxes can be estimated from the difference in the BSR and seafloor temperatures and the average sediment thermal conductivity (Grevemeyer & Villinger, 2001; Chi & Reed, 2008). A comparison of this BSR-derived temperature field to a topography-derived, conductive heat flow model will highlight perturbations to the background thermal structure that could help constrain the style, location and magnitude of fluid flow in a dense lateral spacing (Fisher & Hounslow, 1990; Zwart et al., 1996).

In this study, we use multi-channel seismic (MCS) reflection data, collected offshore SW Taiwan, to determine the along-profile BSR depth and derive spatially-dense (6.25 to 12.5 m lateral spacing along the profiles) temperature field information. We compare the BSR-derived temperature field to the output of a 2D steady-state conductive-only numerical model of the subbottom temperature. We interpret discrepancies between the models as resulting from localized temperature perturbations driven by upward focused fluid flow along dipping conduits into the gas hydrate stability zone (GHSZ). We develop a method to quantify the fluid flow rate based on the BSR-derived temperature field and apply it to the Manila Trench offshore SW Taiwan. From these results, we investigate the regional partitioning of focused and diffusive fluid flow across the Taiwan accretionary wedge from subduction in the south to collision in the north. We found fluid migration patterns vary both in space, and very likely in time, when the crust evolves during orogeny. The method we present in this study to quantify fluid fluxes is applicable to a range of tectonic regimes and can provide critical insight into local and regional fluid flow.

2. Geological Setting and Gas Hydrate Accumulation

Offshore southwestern Taiwan is among the best places to investigate lateral variations of fluid flow due to its geological setting, dense coverage of MCS data, and ample presence of gas hydrates across the region. The convergence zone offshore SW Taiwan is located along the boundary between the Eurasian plate and the Philippine Sea Plate (PSP), where the South China Sea (SCS) lithosphere is subducting eastwards beneath the PSP at the Manila Trench. The subduction system transforms into an incipient arc-continent collision system from south to north, as the subduction complex encroaches on the passive China continental margin (Teng, 1990). The orogeny is believed started since 4-6 Ma (Suppe, 1984; Teng, 1990) and is currently very active with a convergence rate of 7-9 cm yr^{-1} a direction of N54◦W (Figure 1). This geometry makes it possible to apply the concept of time-space equivalence to study crustal structure and fluid flow pattern from the younger stage in the south to a mature stage in the north. In addition, due to the high convergence rate, the deformation in the accretionary wedge is fast and large. The Taiwan accretionary wedge consists of three distinct structural domains (Reed et al., 1992) from west to east: (1) the lower slope near the Manila Trench, (2) the upper slope, and (3) the backthrust domain near the Luzon Arc. In this study, we focus mainly on the lower slope, which is further divided into frontal and rear segments (Lin et al., 2009). The frontal segment is mostly composed of west-vergent elongated anticlinal ridges with underlying blind thrusts. The rear segment is associated with asymmetric west-vergent ridges as well as many emergent and imbricate thrusts, which have tilted the hanging wall strata.

Researchers performed extensive seismic surveying within the Taiwan accretionary margin over the past two decades (Chi et al., 1998; Liu et al., 2006; Schnürle et al., 2011; Reed & Liu, 2014). This information was essential for describing the local and regional tectonic regimes within the prism, identifying important geologic features (e.g. faults and mud diapirs) and studying the distribution of gas hydrates. The subset of MCS data used in this study (Figure 1; red lines) covers the entire lower and upper slopes of the prism to both the north and south with an approximate spacing of <8 km.

There is ample evidence of the occurrence of gas hydrate offshore SW Taiwan. At large scales, BSRs cover an area of more than 15000 km^2 (Chi et al., 1998, Liu et al., 2006; Chi & Reed, 2008). In addition, Berndt et al. (2019) investigated the geological controls on gas hydrates using various geophysical techniques, while geochemical data derived from sediment cores identified hydrate related fluid venting in the region (e.g., Chuang et al., 2010). Finally, gas hydrate has been sampled in the active continental margin (MOST, 2018). Due to its geological setting and the comprehensive database of seismic reflection profiles, Taiwan’s accretionary prism provides a unique opportunity to study hydrology and fluid migration rates systematically along an entire convergent plate boundary.

[Figure1]

3. Data and Methods

3.1 BSR-derived temperature field

We use the BSR depth in seismic data to estimate the subsurface temperature field, geothermal gradient, and heat flow in a regional framework (e.g. Shipley, 1979; Zwart et al., 1996). More details on this calculation are included in the Appendix A.

3.2 The 2D conductive temperature field

We numerically calculate subsurface temperatures using a 2D finite element method adopted from Chen et al. (2014) and Kunath et al. (2020); this model solves the 2D conductive heat transport equation and fully accounts for the 2D topographic effect (Carslaw & Jaeger, 1959). We use 2D seismic data and the BSR-derived temperature field in the study area to constrain the model geometry and geothermal gradient across the region, respectively. We assign a constant seafloor temperature using the combination of an empirical relationship between depth and temperature in the region (Chi & Reed, 2008) and in-situ thermal probe measurements. We impose no flow boundary conditions to the model edges and a constant temperature at the flat base of the model. The lower part of the model is for numerical analysis only; our focus is on the shallow region (<2000 mbsl) where the topographic effects are strong and where the BSR is located. The result is a first-order 2D temperature field along the seismic profile assuming purely conductive heat transfer and accounting for topographic effects. For the complete model derivation, refer to the appendix B.

Figure B.1 shows an example of the model output from the Yung-An Ridge. The output indicates that, in a purely conductive system, the temperature field changes nearly homogeneously with depth, with slight variations that mimic the seafloor topography; these variations become muted in the deeper sections. A comparison between the expected BSR depth from these 2D steady-state calculations with the observed BSR depth reveals locations of elevated temperatures along the seismic profiles.

3.3 2D fluid flow rates derived from localized heat flow anomalies

We derive a 2D model of focused fluid flow, and related heat transport, along structural and lithological conduits to estimate the 2D subbottom temperature accounting for localized advection.

The model consists of a thin, permeable, dipping structure that crosscuts a homogenous impermeable medium (Figure 2a). Warm fluid flows upward along the conduit, bringing additional heat to the system that creates temperature anomalies in the sediment bordering the conduit, relative to the conductive-only model. We assume that (1) the fluid entering the conduit (x = 0) is equal to the ambient temperature, estimated from our 2D steady-state conductive model. Moreover, this fluid flow is assumed to have contributed to the shallow thermal structure at a wavelength defined by the local BSR depth variations on the scale of hundreds-of-meters within the fault outcrop, where the inferred heat flow is increased. We also assume that: 2) the conduit and surrounding sediment have constant geophysical properties; and 3) a constant conduit thickness of one meter. The 4) lateral conduction of heat is assumed negligible; thus, the conduit dip angle (φ) must not be too large, probably < 30-40° (Vasseur et al., 1993). We used the outputs from our 2D conductive only model as the constraints to model temperature along the conduit with the given geometry of the conduit, the geothermal gradient, and the fluid flux.

The steady-state temperature disturbance (ΔT) related to fluid flow along the conduit has the following analytical solution (Vasseur et al., 1993):

$$\Delta T(x) = \frac{Pe\ y\ tan(\varphi)}{1-Pe\ tan(\varphi)}\left[\ h(x) - h_0\left(\frac{h0}{h(x)}\right)^{-\frac{1}{Pe\ tan(\varphi)}}\right]. \qquad (1)$$

In Equation 1, Pe is the dimensionless Peclet number ($Pe = q\rho_f c_f/k$), y is the undisturbed geothermal gradient (dT/dz; °C m^{-1}), and h_0 and h are the subbottom depth to the base of the conduit and along-conduit depth (m), respectively. Pe describes the ratio of the advective and diffusive transport rates and is a function of the thermal conductivity (k; W m^{-1} K^{-1}), the fluid density (p_f; kg m^{-3}), the thermal heat capacity of the fluid (c_f; J kg^{-1} K^{-1}), and the fluid flow rate along strike (q; m^3 yr^{-1} m^{-1}).

Equation 1 gives the temperature perturbation, relative to steady state conductive conditions, due to fluid flow along the conduit due to a specified fluid flux. The total temperature along the conduit is determined and forms the new lower boundary condition. Then we add the temperature field on the bathymetry as the top boundary condition before we solve for the 2D temperature field simultaneously.

We ran the model at dimensionless flow rates ($Pe \tan\varphi$) ranging from 0.1 to 30 and compared them to the purely conductive case ($Pe \tan\varphi = 0$) to investigate the thermal effect of localized fluid flow on the gas hydrate system (Figure 2b and c). As warm water flows along the conduit, temperatures will increase in the bounding sediment conduit, leading to a lateral varying isotherm shoaling towards the fault (Figure 2b). The normalized temperature disturbance ($\Delta T' = \Delta T/h_0\gamma$) relative to the normalized lateral distance along the fault ($x' = xtan(\varphi)/h$) indicates that the degree of disturbance is asymmetric (Figure 2c). At $Pe \tan\varphi < 0.5$, $\Delta T'$ is greatest near the source, while, at $Pe \tan\varphi > 0.5$, $\Delta T'$ is greatest near the point of furthest intrusion. As temperature is one of the primary controls on gas hydrate stability, these flow-derived thermal anomalies may control the local depth of the GHSZ, which would be reflected in observed depth to the BSR in sediments proximal to the conduits.

[FIGURE2]

We develop a method to estimate fluid flow rates through permeable conduits by combining the results from our 2D conductive and advective thermal models with the observed BSR depths. We solve Eq. (1) for different source depths and flow rates and then calculate the normalized misfit between the observed and modeled temperature fields. We then perform a grid search over the range of models to find the parameters that minimize the misfit. This method provides a simple and efficient estimation of the fluid flow rate through the conduit.

4. Results

4.1 Performance test on ODP Leg 142 Site 892

To validate our new method, we first apply it to ODP Leg 142 Site 892 in the Cascadia accretionary wedge off Oregon (Westbrook et al., 1994). Site 892 drills through the hanging wall of and penetrates through a thrust fault (Figure 3a). There is a well-defined regional BSR that deflects towards the seafloor in response to the upward flow of warm fluids along the fault. We chose this site because borehole data provide an excellent thermal constraint on the hydrology and rare direct measurements of fluid discharge rates from seafloor measurements (Linke et al., 1994; Westbrook et al., 1994). In addition, analytical and numerical models provide good constraints on the flow rates from thermal and geochemical anomalies along the fault zone (Davis et al., 1995; Screaton et al., 1995; Mann & Kukowski, 1999).

[FIGURE3]

We use a geothermal gradient of 54 ^{o}C km^{-1}, based on the water sampler and temperature probe measurements (Westbrook et al., 1994), an average thermal conductivity of 1.04 W m^{-1} K^{-1}, and a seafloor temperature of 4.27 ^{o}C (Zwart et al., 1996). The imaged fault is visible as a discrete strong reflector to approximately 200 mbsf and has an average dip of 14^{o} (Zwart et al., 1996). We calculated the average temperature field misfit at fluid flow rates and source depths ranging from 0-40 m^{-3} yr^{-1} m^{-1} and 150-250 mbsf, respectively (Figure 3b). The average misfit for a purely conductive geothermal model is 1.8 ^{o}C (Figure 3c), while the advective model reduces the misfit to 0.37 ^{o}C (Figure 3d) when using optimized parameters (red star, Figure 3b) of 29 m^3 yr^{-1} m^{-1} and a source depth of 175 mbsf.

Despite the simplicity of our model, our estimated fluid flow rate and source depth agrees well with results derived from other, more sophisticated studies. For example, Mann and Kukowski (1999) numerically modeled in steady-state and tested for a wide range of material properties. They found that a flow rate of 7 m^3 yr^{-1} m^{-1} and source depth of 200 mbsf provided the best fit to the observed thermal anomalies. Davis et al. (1995) suggested that a fluid flow rate of 32 m^3 yr^{-1} m^{-1} was appropriate, while Screaton et al. (1995) calculated a fluid rate ranging from 17-200 m^3 yr^{-1} m^{-1}. As our modeled optimal parameters, 29 m^3 yr^{-1} m^{-1} and 175 mbsf, agree well with these previously published values, we are confident that our model can be applied to other locations where direct flow measurements are not available.

4.2 Estimates of 2D fluid flow rates offshore SW Taiwan

We apply our method to several sites offshore SW Taiwan in the accretionary wedge where there is high-density MCS coverage (Figure 1). We first use the BSR depth to estimate the geothermal gradient across the region (Figure 4); geothermal gradients range from 30 – 120 ^{o}C km^{-1}. In much of the study area, the BSR-derived and conduction-only modeled geothermal gradients match well and track predictably with the seafloor topography (Figure 5a; Ridges 2 and 3). In several cases, however, there are spatial perturbations in the geothermal gradient on the scale of hundreds-of-meters (Figure 5; Ridge 1). We interpreted these perturbations, when observed at the intersection with structural and lithological discontinuities, as evidence of focused fluid flow into the GHSZ. We identified similar perturbations at 23 sites in the region and have estimated fluid flow rates at each of them (Figure 4; Table S.1).

[Figure4 & 5]

Three sites close to the deformation front had discharge rates between 10-16 $m^3\ yr^{-1}\ m^{-1}$ (Figure 4). These three sites spatially coincide with regions where Chi and Reed (2008) previously reported high heat flow values, potentially related to high fluid flow rates. Twenty-one other sites located along fault- and lithological discontinuities at the intersection between thrust ridges, such as the edge of the slope basin boundary, had low to moderate fluid flow rates ranging from 0.1-7 $m^3\ yr^{-1}\ m^{-1}$, with slower rates generally attributed to slope basin discontinuities (<2.5 $m^3\ yr^{-1}\ m^{-1}$). In addition, our results suggest that the fluid flow along the faults are about 2 to 15 times higher than that along the base of the slope basin. Therefore, we interpret that the geologic conditions act as an important constraint on the fluid flow rate and, thus, the potential local thermal perturbation. Figures 6 and 7 show examples of the fluid flow rate calculations for the two predominate conduit types: faults (Figure 6) and slope basin boundaries (Figure 7).

At Yung-An-Ridge (Figure 6), the depth and the lateral extent of the modelled conductive-only BSR differs from that of the BSR observed in the seismic data (Figure 6a). This depth discrepancy is the greatest in the hanging wall of the fault, where the mapped BSR is tens of meters shallower than the theoretical BSR. The average temperature and geothermal gradient discrepancies between the 2D conductive-only temperature field and the BSR-derived temperature are 1.6 ^{o}C and 5.7 $^{o}C\ km^{-1}$ (Figure 6c). Our advection model (section 3.3) indicates an optimal source depth and flow rate of 1875 mbsf and 3 $m^3\ yr^{-1}\ m^{-1}$, respectively (Figure 6d). As a result, when accounting for the advection of warm fluid along the fault, our model reduces the average temperature misfit along BSR to 0.37^{o}C (Figure 6b) and geothermal gradient misfit to 1.2 ^{o}C km^{-1} (Figure 6c).

[Figure6]

At Four-Way-Closure Ridge (Figure 7), seismic data show a pronounced BSR shoaling up to 15 m at the edge of the slope basin boundary (Figure 7a). The average temperature and geothermal gradient discrepancies between the 2D conductive-only temperature field and the BSR-derived temperature are 1 ^{o}C and 3.5 ^{o}C km^{-1} (Figure 7c). Our advection model indicates an optimal source depth and flow rate of 550 mbsf and 2 m^{3} yr^{-1} m^{-1}, respectively (Figure 7d). As a result, when accounting for the advection of fluid flow along the base of the slope basin, our model reduces the average temperature misfit along BSR to 0.25^{o}C (Figure 7b) and geothermal gradient misfit to 1.2 ^{o}C km^{-1} (Figure 7c). In addition, heat probe data at the seafloor close to the edge of the slope basin show a high geothermal gradient (55.9 ^{o}C km^{-1}; black cross in figure 7c) compared to the BSR-derived temperature gradient (48 ^{o}C km^{-1}), that is a 7.9 ^{o}C km^{-1} discrepancy. This temperature anomaly gives us additional independent evidence for focused fluid flow into the GHSZ because focused flow along the base of the slope basin increases the temperature in the sediments above the proposed conduit. Our advection model reduces the geothermal gradient misfit to the heat probe data to 1.4 ^{o}C km^{-1}.

[Figure7]

4.3 Fluid budget of Taiwan’s accretionary wedge

We estimate the total fluid budget along three seismic transects that generally run east-west across Taiwan’s accretionary prism using an approach adopted from Townend (1997) and Pecher et al. (2010); these budget calculations are constrained by porosity values derived from published seismic velocities and the thickness of the sediment column above the decollement at the deformation front (Appendix C; Table C1;). We use seismic line T2933 (EW9509-2933, McIntosh et al., 2013) and L10 (MGL0905-10, Deng et al., 2012) as representative transects for the initial-collision zone in the northern portion of the wedge, and used line L27 (MGL0905-27, Lester et al., 2013) to represent the subduction zone in the south.

The fluid budget in accretionary prisms consists of four interconnected source and sink terms (Townend, 1997; Figure 8). Sources include a) fluid accreted into prism (v_{accr}); b) fluid produced via smectite-illite transformation (v_{hydac}). Sinks are c) fluid expelled from the wedge (v_{comp}) via either focused discharge (c_1) or other processes (c_2; e.g. diffusive flow, sediment compaction). The last component is the fluid remaining in the sediment (d).

The fluid budget from the incoming plate (a) to the north along transect T2933 is with 65. 82 m^3 yr^{-1} m^{-1} about 150% of the southern transects (Table 1), due to thicker incoming sediment and higher sediment porosity of the northern transect closer to the sediment sources onland (Table C1).

For the contribution from smectite-illite conversions (b), the two northern transects are estimated at 9.8 - 9.9 m^3 yr^{-1} m^{-1}, which is slightly higher than the southern transect (7.45 m^3 yr^{-1} m^{-1}), also due to its thicker sediment. Overall, there are more sources of fluid for the northernmost transect. The total dewatering flux (c) is at 27-41 m^3 yr^{-1} m^{-1} for the two northern transects and at 25 m^3 yr^{-1} m^{-1} for the transect further to the south.

We calculated the focused discharge budget (c_1) along transects T2933 (A to A’ in Figure 4), L27 (B to B’) and L10 (C to C’). For the transect T2933, we found temperature evidence of focused fluid flow zones along three faults, and two along the base of the slope basin (Figure 4 and 8b). For the L10 transect, evidence for localized fluid flow is observed at two fault zones and one along the base of the slope basin (Figure 4 and 8c). For the southern transect (L27), evidence of focused fluid flow zones is found along three faults close to deformation front (Figure 4 and 8d). For all transects, we first averaged the fluid flow rates along the ridge, then we summed the fluid flow rates from multiple fluid conduits (five in the northernmost transect, and three in the other two transects) to get the total discharge rates. We found the focused discharge for the northernmost transect (T2933), 19.55 $m^3\ yr^{-1}\ m^{-1}$, is three times higher than that of the southern transect L27 (6.5 $m^3\ yr^{-1}\ m^{-1}$) (Table 1). The focused discharge rate for transect L10 is 8.25 $m^3\ yr^{-1}\ m^{-1}$.

The last component of the fluid balance equation is the fluid remaining in the wedge (d). It is estimated by subtracting the discharge rate ($c = c_1 + c_2$) from the sum of the fluid from the incoming plate and from the smectite transformation. The fluid remaining within the subducting sediments is estimated at 34.22 $m^3\ yr^{-1}\ m^{-1}$ for the northernmost transect and at around 25 $m^3\ yr^{-1}\ m^{-1}$ for the other two transects.

The results show that the fluid partitioning ratio between focused and diffusive flow (e) and the dewatering flux to the seafloor through focused fluid conduits (e_1) along Taiwan's accretionary prism are spatially varying. The partition ratio (e) for the northernmost transect T2933 is with 0.98 about twice that of the transect L10, and three times that of transect L27.

The average dewatering flux through focused fluid conduits (e_1) is 26% in the southern transect and 38.5% in the northern transects. The maximum 47% in the collision zone in northernmost transect is slightly higher than the 26% subduction zone in the south.

[Figure8]

[Table1]

5. Discussion

5.1 Potential sources of uncertainty

There are potential sources of uncertainty that may affect our model results; these mostly consist of errors both associated with the model parameters and with the assessment of BSR-derived temperature, and factors affecting shallow thermal structures. The major sources of uncertainty in our model include: 1) the depth-dependent velocity, porosity, and thermal conductivity relationships; 2) BSR subbottom depth estimates; and 3) environmental disturbances to the near-surface temperature field. Most of these factors, have been addressed in detail (e.g. Yamano et al., 1992; Grevemeyer & Villinger, 2001). Also, specifically for the Taiwan region, Chi and Reed (2008) studied the factors requiring consideration when using a BSR to study the shallow thermal structures off SW Taiwan. Here, we briefly address these uncertainties.

We modeled the first-order temperature field pattern assuming a homogenous sedimentary section with constant thermal conductivity. This assumption, however, is obviously an oversimplification as the sediment thermal properties will be heterogeneous at different spatial scales due to either changes in porosity or heterogeneous lithology. Sediment burial increases the surrounding pressure and forces the sediment to undergo compaction, reducing the porosity and raising the bulk thermal conductivity. In addition, since the bulk conductivity is a function of the individual conductivities of the minerals, sediment compositional changes will result in predictable changes in the bulk conductivity. However, since our study area focused on a region relatively close to the seafloor, where strata and thermal properties are mostly sub-parallel to the seafloor, it is likely that the effects of both of the factors are significantly minimized (Villinger et al., 2010). We should be able to define the first-order thermal patterns with relative confidence.

We derive the BSR subbottom depth and the fault geometry using the empirical Hamilton equation (Hamilton, 1980). Grevemeyer and Villinger (2001) estimated that the uncertainty of velocity function on BSR derived heat flow ranges between 5-30%. For the Taiwanese data set that have been acquired for our study area, Chi and Reed (2008) did a multitude of sensitivity tests and showed that, for an arbitrary 30% error in the Hamilton-derived velocity estimate, the geothermal gradient only changes by 0.5 – 2.5 ^{o}C km^{-1}, which is relatively small. Fortunately, the error in subbottom velocities has an opposing effects on the BSR temperature and BSR subbottom depth, resulting in a near-neutral cumulative error in the geothermal gradient.

We calculate the temperature at the BSR using an empirical P-T hydrate stability curve, assuming that pore fluid pressures are hydrostatic. The compressional nature and diverse lithology of accretionary wedges, however, make pore pressure predication difficult and increase the likelihood of localized elevated pore pressures. Anomalous high pore pressures in the sedimentary strata of the anticlines may shift the BSR downwards (Tinivella & Giustiniani, 2013), causing misinterpretation of features at the BSR. Our data is not suited to identify zones of overpressure. However, as overpressure would force the base of the GHSZ deeper, the discrepancy between the observed and expected BSR depth would only increase. As a result, the fluid flow rate required to minimize the misfit would be greater than in the hydrostatic pressure case.

Frictional heating effects resulting from movement along the fault zone (Fulton et al., 2013; England, 2018) might be a possible thermal disturbance that may be masquerading as advective fluid flow. However, because frictional heat is proportional to the depth through the stress gradient, we expect no significant contribution of frictional heating at a scale a few hundred meters near the fault outcrop. Nonetheless, we evaluated the potential role of frictional heat on the temperature anomaly along the Yung-An Ridge profile, as shown in Figure 9. Since no large earthquakes occurred near our study sites, our attention is on thermal signals from frictional heating from slip events occurring over long geological time scales as proposed by Molnar and England (1990) (Appendix D). The theoretical temperature gradients show the effect on the predicted temperature anomaly for a range of realistic shear stresses in convergent plate boundaries (0 to 30 MPa km^{-1}) and slip rates of 40 and 80 mm yr^{-1}. The theoretical temperature gradients decrease due to under thrusting of the cold footwall block near the fault trace, except for larger stress gradients (i.e., 30 MPa km $^{-1}$), and then increase at larger distances due to the frictional heating related to the stress gradient. Since our observed temperature signature increases towards the fault at a scale of hundreds-of-meters where the effects from frictional heating on the temperature signature should be small (Figure D. 1), we are confident that frictional heat presents no large impediment to determining fluid flow rates from BSR temperature.

[Figure9]

Our model considers the steady-state topographic effects on the heat transfer. A number of other transient processes (e.g. deposition, erosion, uplift, mass wasting events), however, may contribute to topographic changes that are unaccounted for in a static seismic profile. These processes may alter pressure profiles and heat flow patterns within the sediment that alter the hydrate stability conditions at depth (Hornbach et al., 2008). These changes, however, are often spatially and temporally longer wavelength variations that are distinct from the effects of focused flow. In addition, information from seismic profiles might show evidences of such seafloor topographic changes, allowing better interpretation of the temperature data.

Overall, despite these uncertainties in our model, focused fluid flow is likely the primary cause for the localized BSR-derived heat flow anomalies when they are restricted to localized structures such as fault zones (Carson & Screaton, 1998). Given the direct focus of our model on this heat flow mechanism and the convincing agreement between our results from ODP Site 892 and those from other studies, we are confident that our model provides a decent order-of-magnitude estimate of the fluid flow rates.

5.2 Time averaged fluid flow rates

Active fluid flow along structural or lithological conduits may be heterogeneous and transient over time scales of days to years – or tens of thousands of years (Fisher & Hounslow, 1990; Brown et al. 2005; Davis et al., 2006; Davis & Villinger, 2006; Solomon et al., 2009; Saffer & Tobin, 2011). Overall, we document similar ranges to those reported focused flow rates from other margins (e.g. Minshull & White, 1989; Davis et al., 1992; Linke et al. 1994; Carson & Screaton, 1998; Mann & Kukowski et al., 1999; Hensen et al. 2004; Ranero et al., 2008; Pecher et al., 2010; Saffer & Tobin, 2011). However, our model cannot explicitly consider temporal and spatial variations in hydrological parameters. Nonetheless, for most of our study sites, the thermal anomaly obtained from our forward modelling matches the anomaly determined from the BSR depth very closely, thus the steady state model appears adequate in our case.

The focused fluid flow rates obtained from our BSR-based model likely represent the average rate of flow along the fault over a considerable period of time. Thus, it is unsurprising that other studies, using shorter time scale methods, have documented different time scales of fluid flux. For example, our BSR-derived fluid flow velocities are one to two orders of magnitude smaller than those required to match the transient temperature anomalies observed within the borehole (Davis et al., 1992), or measured by flow meters mounted at the seafloor within the region (Linke et al., 2004). Thus, the time-averaged temperature field may be very different from the instantaneous, transient temperature fields that tend to have shorter spatial wavelengths changes.

5.3 Models of fluid budget and focused flow rates along Taiwan's accretionary prism

The fluid migration patterns along the Taiwan accretionary wedge might vary both spatially, and likely temporarily, due to its geometry – the tectonic evolution from subduction to collision. In our case, fluid production and dewatering rates are increased from subduction to collision (Table 1). A similar pattern is observed in the fluid advection, as focused fluid conduits channeling on average 38.5% (maximum up to 47%) of the total dewatering flux (e_1) in the collision zone and 26% in the subduction zone. Overall, these estimates are slightly larger than results from previous modeling studies from other margins using different methods (Ranero et al., 2008; Lauer & Saffer, 2012; von Huene et al., 1998; Towned et al., 1997; Pecher et al., 2010; Ellis et al., 2015). For example, cumulative dewatering rates from seismically derived porosity reduction are between 20 – 39 $m^3\ yr^{-1}\ m^{-1}$ for the Hikurangi margin (Towned et al., 1997; Pecher et al., 2010; Ellis et al., 2015) and 8 $m^3\ yr^{-1}\ m^{-1}$ for the Alaska margin, occurring within 14 km landward of the trench (von Huene et al., 1998). Modeling studies at these margins also indicate that 5 - 35% of the incoming fluids escaped by focused flow (Ranero et al., 2008; Lauer & Saffer, 2012; Ellis et al., 2015), while the remaining fluids escaped via diffusive flow across the seafloor (Carson & Screaton, 1998).

These differences in fluid flow patterns between our transects, and between other convergent margins, can be attributed to differences in the initial sediment thickness, initial porosity and total porosity reduction during accretion, and the convergence rate, which together govern rate of fluid production and dewatering. Taiwan is a highly active tectonic region, with high convergence rate, stronger onshore erosion, and offshore deposition, which could drive stronger fluid advection from depth. In addition, the intensive deformation when the thicker Chinese passive margin enters the convergent boundary with the Philippine Sea plate and subduction changes into arc-continent collision may assist in fault formation or reactivation or in the development of structures that support focused fluid flow.

The presence of high fluid flow rates at individual sites near the toe of the prism is striking (Figure 4); these rates are consistent with more intense dewatering near the toe of other accretionary prisms (e.g. Moore et al., 1998; Moore & Vrolijk, 1992). Still, localized fluid expulsion rates of up to 10.5 and 16 m^3 yr^{-1} m^{-1} are high compared to the total dewatering flux (c) of 41.4 m^3 yr^{-1} m^{-1} (northern transect) and ~25 m^3 yr^{-1} m^{-1} (southern transect), respectively. This would imply that, at individual sites, between 25-60% of the total dewatering budget of the prism are funneled through the decollement. It is clear, however, that there might be dramatic variations in the fluid flow pattern along strike. For example, field observations reported from other margins document localized seafloor vent sites rather than continuous seepage along fault traces (e.g. Hensen et al., 2004). As such, the flow rates reported by our model may not be sustained at all locations along a given fault outcrop. Although, the sites where we modeled flow rates typically coincide with high regional geothermal gradients (Chi & Reed, 2008), suggesting that larger scale processes may affect the heat flow pattern there. In addition, the seismic data used in this study cover a large area and adjacent seismic profiles usually show similar patterns along the strike.

Along-strike flow patterns may contribute to increased localized focused fluid flow rates, which cannot be fully captured by 2D models. For example, recent 3D seismic imaging, together with mapping of seismic attributes along fault surfaces, have begun to highlight the importance of trench-parallel fluid flow (Shipley et al., 1997; Bangs et al., 2015). In these cases, fluids flow tens of kilometers along strike and up-dip direction, rather than flowing perpendicular to the trench and along the largest gradients in driving forces and rock and fluid properties. For the Taiwan region, similar heterogeneity in the subsurface flow pattern is likely important, but the three-dimensionality of the flow systems remains poorly constrained.

In summary, modeled focused fluid flow rates demonstrate the efficiency of faults in channeling fluids and heat towards the seafloor. Additionally, our simplified calculation of the fluid budget suggests that fault zones may play an important role in the fluid budget of the convergent boundary offshore SW Taiwan. Fluids that are guided towards the GHSZ have the potential to influence gas hydrate formation and saturation at localized sites, because fluids that are pressure gradient driven and carrying heat are more likely to enter the GHSZ, where they could be incorporated into hydrates if conditions allow. Deformation and its associated faulting are probably a key process in facilitating fluid migration from depth and may become increasingly significant when prospecting for gas hydrates.

5.4 Implication for other geological processes

Temperature measurements from a borehole that penetrates the fault or surface measurements directly above faults can help to quantify frictional resistance during fast and slow slip events or other in-situ properties relevant to understanding fault or earthquake processes because most of the frictional resistance is dissipated by heat processes (Fulton et al., 2013; England, 2018; and references therein). However, there is also the possibility that other processes at depth might affect the thermal structure, which must be considered when interpreting the temperature recordings. Our results suggest that the long-term frictional heart source from faulting might not be the main factor controlling the shallow thermal structure at hundreds-of-meters scale near the fluid conduit (Fig 9); even though it may take place elsewhere along this and other convergent boundaries (England, 2018). In case of a short-term (coseismic) frictional heat source due to the earthquake fault slip, the short wavelength heat pulse would occur over the entire ruptured surface on the fault. However, such short wavelength heat pulse will diffuse into longer wavelength and dissipate over time. Multiple slips on the fault over long period of time (million years) are what we are studying in this work.

The use of long-term measurements to monitor evolution of thermal anomalies over time would allow separation of hydrogeological and frictional heating signals (Fulton et al., 2010), but most of the offshore and mountainous regions within convergent boundaries usually have sparse heat flow data due to the limited access and high costs. As a result, observations from localized measurements are often extended outwards for hundreds of meters to several kilometers laterally. However, our results also illustrate that data from localized measurements may not be fully representative of the regional thermal processes, but influenced by localized fluid flow processes and bathymetry. Meanwhile, we have presented a method to develop a densely sampled temperature field using the observed seafloor topography and BSR depth in MCS profiles. This method not only provides us with spatially relevant insight into the regional heat flow patterns, but also allows us to identify regions where localized processes may be disrupting that regional pattern. In addition, we have then developed a method to translate those localized disturbances into time-averaged fluid flow rates. Clearly, densely sampled temperature measurements are advantageous in improving the interpretation of related temperature observations and various geological processes, including faulting, topographic effects and fluid flow.

6. Conclusions

Many convergent margins have bottom simulating reflectors that deflect towards the seafloor, indicating localized variations in the hydrate stability conditions. These variations, when observed near structural and lithological fluid conduits, may be explained by focused fluid flow transporting warmer fluids to shallower depths.

We have developed a rapid method to quantify the first-order fluid migration patterns and rates to investigate how heat advection along these fluid conduits interacts with the overlying gas hydrate system. We derived the regional temperature field from the observed BSR depth or from in-situ heat probe measurements and compared the results to a 2D steady-state conduction-only thermal model to estimate time-averaged fluid flow rates along dipping conduits. We identified 23 sites of focused fluid flow off SW Taiwan and calculated fluid flow rates between 0.1 to 16 $m^3 yr^{-1} m^{-1}$, with highest rates within the thrust faults near the toe of the accretionary prism and relatively lower rates along lithological discontinuities such as the base of the slope basin. These results provide one of the most comprehensive focused fluid flow studies along a particular convergent boundary**.**

We have derived a model of fluid budget for a northern transect in the initial collision zone and a southern transect in the younger subduction zone. By adding time dimension to the regional 2D seismic data, we provided a quantitative link between subduction-collision system evolution, fluid budgets and flow rates in a spatial scale of hundreds of kilometers. Our results highlight that stronger fluid advection from depth occurs across the initial collision zone, as on average 38.5% of the total volume of water subsequently released during compaction of the accretionary prism is expelled at the seafloor through focused fluid flow for the northern transects, which is slightly higher than the 25% for the southern transect. We conclude that focused fluid flow plays an important role in the overall hydrologic budget of this convergent margin, and that the fluid migration patterns vary both in space, and very likely in time, when the crust evolves during orogeny. This newly developed modeling approach may contribute to our understanding of temperature perturbation and dewatering processes along other convergent boundaries.

Appendix A. BSR-Derived Temperature Field Derivation

We derive the temperature gradient and heat flow at BSR depth using the following relation:

$$Q = -k(z)\frac{T_{BSR}-T_{SF}}{Z_{BSR}-Z_{SF}} \quad , \qquad \text{(A1)}$$

Q is heat flow in W m^{-2}, k is the sediment thermal conductivity in W m^{-1} K^{-1}, T_{BSR} is the temperature at the BSR in ^{o}C, T_{SF} is temperature at the seafloor, Z_{BSR} is the depth of the BSR and Z_{SF} is the depth of the seafloor (see Figure A.1). Seafloor and BSR depth are extracted from the depth-migrated seismic data or depth-converted time domain seismic data using the velocity-depth relationship published by Hamilton (1980):

$$Z_{BSR} = V_{AVG} * t_{owt} \qquad \text{(A2)}$$

$$Z_{BSR} = [1.511 + (1.041 * t_{owt}) - (372 * {t_{owt}}^{2})] * t_{owt} \ ,$$

V_{AVG} is the average velocity of the sediments above the BSR in m s^{-1}, and t_{owt} is the one way travel time of BSR subbottom depth in seconds. Temperature at the BSR was obtained from the methane hydrate phase boundary using the software Heriot-Watt Hydrate (HWHYD), developed at Heriot-Watt University, assuming hydrostatic pressure and seawater. The assumption of methane for hydrate formation is based on geochemical analyses of a number of seafloor cores from off SW Taiwan (Chuang et al., 2010). Thermal conductivity values are from conductivity-temperature-depth readings from the region of our study area (Shyu et al., 2006). We estimate temperature at the sediment water interface based on an equation (Chi & Reed, 2008) derived by least square fitting the water temperature and depth data provided by the National Ocean Research of Taiwan:

$$T_{SF} = 0.2597 * (LnZ_{SF})^3 - 3.802 * (LnZ_{SF})^2 + 10.67 * (LnZ_{SF}) + 26.96 , \qquad \text{(A3)}$$

LnZ_{SF} is the natural log of water depth. The water depth in the study region ranges from 600 to 3700 m and T_{SF} ranges from 2.0 to 7.5 °C assuming the temperature on the seafloor sediment is similar to that of the seawater.

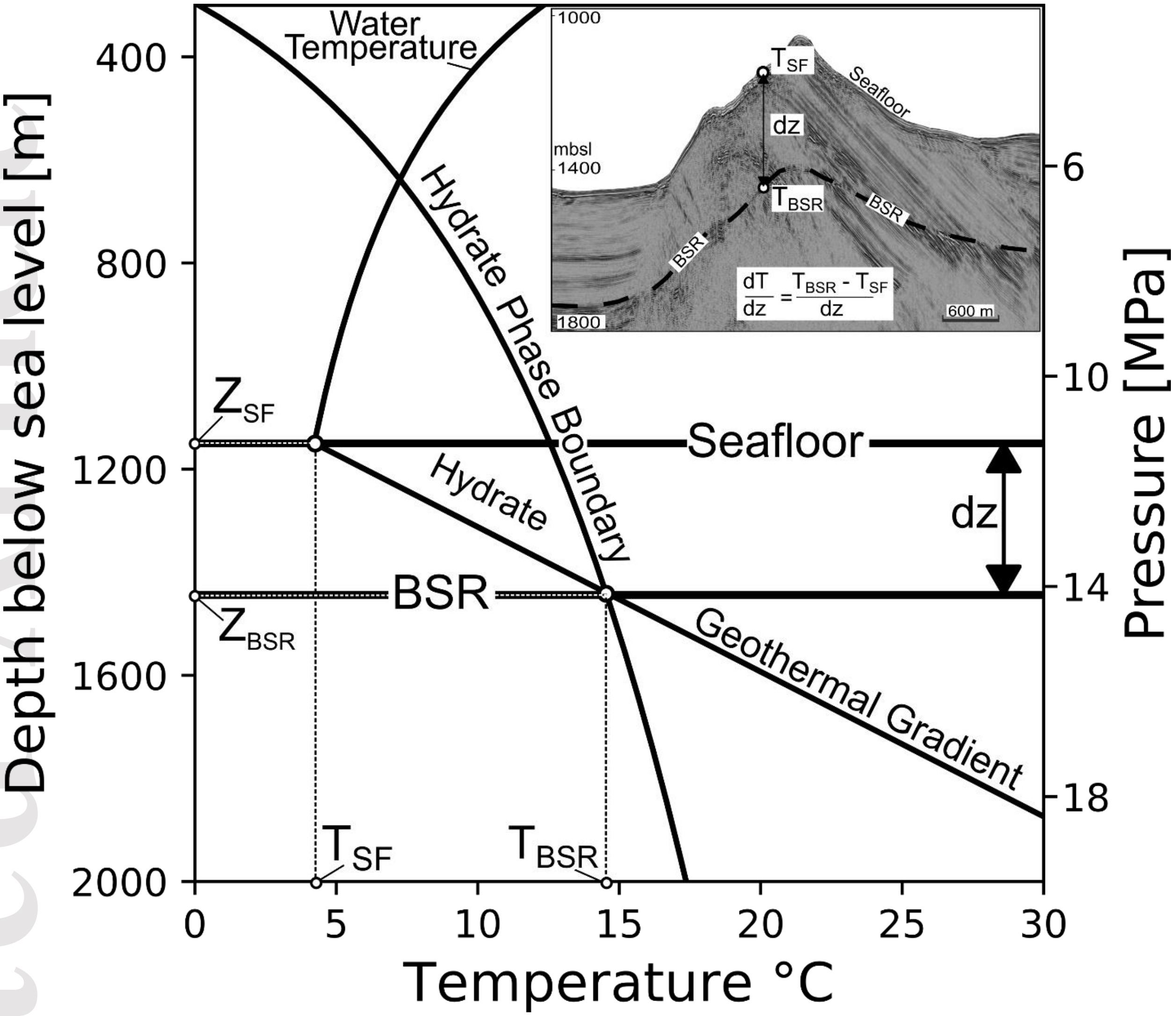

Figure A. 1. The gas hydrate phase boundary for pure methane in seawater, used for calculating the geothermal gradient. Z_{SF} and Z_{BSR} and T_{SF} and Z_{BSR} are pressure-temperature points extracted from the seafloor and BSR depth as highlighted in the inset (double sided arrow). These values are then used to estimate the subsurface temperature field, geothermal gradient, and heat flow in the region.

Appendix B. 2D Conductive Temperature Field Derivation

To calculate subsurface temperatures, we use a 2D finite element model that solves the 2D conductive heat transport equation and fully accounts for the 2D topographic effect (Jaeger & Carslaw, 1959):

$$\rho c \left(\frac{\partial T}{\partial t}\right) = \frac{\partial}{\partial x} k \frac{\partial T}{\partial x} + \frac{\partial}{\partial z} k \frac{\partial T}{\partial z} \ , \qquad \text{(B.1)}$$

where t is the time, T is the temperature, ρ is the average rock density, x and z are the horizontal location along the profile and the depth, respectively, k is the thermal conductivity, and c is the specific heat.

As a first step, we created a triangular mesh on the model domain. We then calculated the steady state heat conduction to estimate the geothermal gradient throughout the model:

$$\nabla \times (k \nabla T) = 0, \qquad \text{(B.2)}$$

This steady-state equation is solved for a regional constant geothermal gradient. We assumed a homogenous sedimentary section (e.g., constant thermal conductivity) due to a lack of representative heterogenous field data with depths in this region. The final temperature field is not dependent on the thermal conductivity used in this steady-state, homogenous modeling. We assigned a constant temperature at seafloor, derived from the equation published by Chi and Reed (2008) or average in-situ thermal probe measurements. We imposed Neumann’s boundary conditions with temperature at the sides increasing linearly with depth below the seafloor without horizontal heat flux across the sides and a constant temperature at the base of the model. The model bottom is flat so its depth must be sufficiently large (~5 km) to avoid artifacts of forcing the temperature contour to be flat near the bottom of the profile. Thus, the vertical dimension of the model is not geologically constrained. To find the regional geothermal gradient, we used the BSR depth where the seafloor has gentler slopes and is less affected by the topography. Once the 2D conductive temperature field was generated throughout the model domain, we tried several different geothermal gradients to minimize the misfit between BSR derived temperatures and the theoretical temperature field in flat topographic regions. The result is a first order 2D temperature field along the 2D seismic profile that considers conductive heat transfer, taking into account topographic effects (Figure B.1).

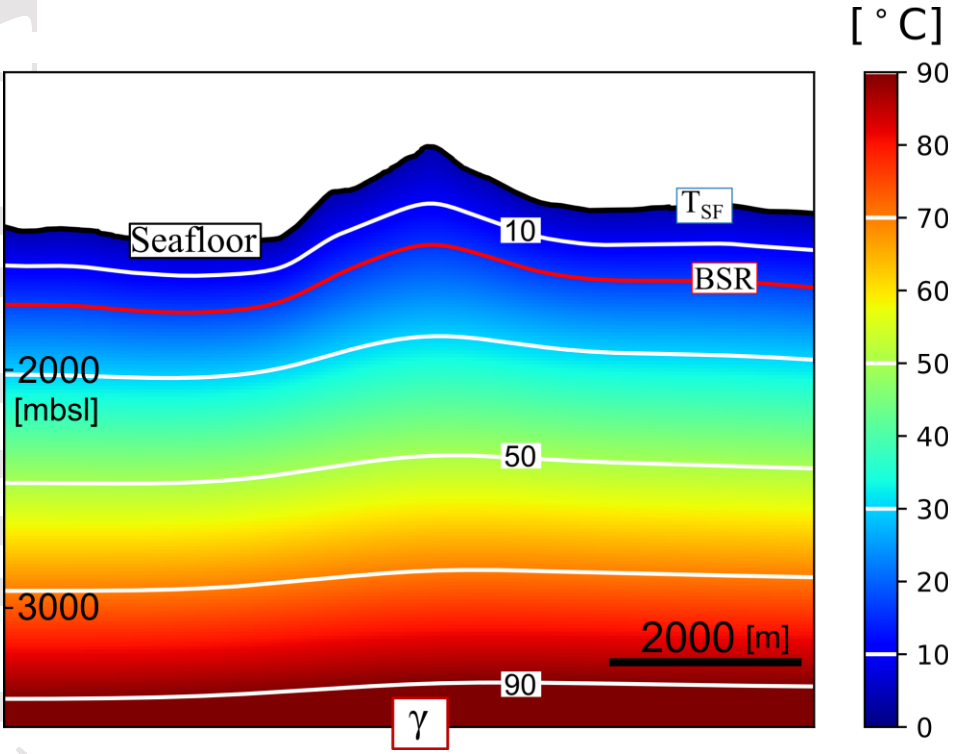

Figure B. 1. 2D steady-state conductive-only numerical model of the temperature field, including topographic effects, using Yung-An Ridge as an example (see Figure 1 for location). The red line shows the predicted BSR depth. The white line represent isotherms as highlighted in the color bar.

Appendix C. Fluid Budget Derivations

We calculate the fluid budget along four seismic transects based on the approach summarized by Townend (1997) and Pecher et al. (2010), where the amount of water volume sediments lose during accretion is constrained by porosity values derived from published seismic velocities.

The volume of pore water accreted into prism (V_{accr}) per time and meter along the margin is calculated as

$$V_{accr} = v * h_{accr} * \phi_{accr} \qquad \text{(C.1)}$$

where h_{accr} refers to average thickness of incoming accreted trench-fill material, v refers to the subduction velocity and ϕ_{accr} is mean porosity prior to accretion.

The volume of water subsequently released during compaction of the accretionary prism (V_{comp}) is

$$V_{comp} = \frac{v * h_{accr} \, (\phi_{accr} - \phi_{comp})}{1 - \phi_{comp}} \qquad \text{(C.2)}$$

where ϕ_{comp} is the mean porosity of the sediments after compaction within the accretionary prism.

The volume of clay-bound water released during smectite dehydration (V_{hydac}) deep in the accretionary prism is

$$V_{hydac} = S * W * v * h_{accr} * (1 - \phi_{accr}) \qquad \text{(C.3)}$$

where S is the volumetric proportion of smectite in the accreted sediment, and W is the volumetric proportion of water in the smectite.

The average porosity of both incoming sediments and final porosity of compacted sediments are constrained by porosity values derived from seismic velocities (Deng et al., 2012; McIntosh et al., 2013; Lester et al., 2013). We used Hamilton (1987) velocity-density relationship for marine sediments, which can be converted to velocity-porosity using the relation $\phi = (\rho - \rho_m)/(\rho_f - \rho_m)$, where ρ is density, ρ_m and ρ_f are grain density and pore fluid density. We used ρ_m = 2700 kg/m^3, and ρ_f of 1000 kg/m^3.

The prescribed parameter values and resulting fluid budget are listed in Table C1. We roughly estimate the error in our fluid budget calculation constraints as < 50 % (20% subduction velocity related, 20% porosity related and 10 – 20% other factors).

Table C.1: Estimate of fluid volumes entering and expelled from Taiwan's accretionary prism for three transects from large offset seismic profiles. Prescribed parameter values and resulting fluid budget are as follows.

	Northern Transects		Southern Transects
Line	T2933[a]	L10[a]	L27[a]
h_{accr} (m)	4000	3300	2870
ϕ_{accr}	32 %	23 %	28 %
ϕ_{comp}	15 %	9.6 %	14 %
v (m/yr)	0.05[b]	0.05[b]	0.05[b]
S	0.20[c]	0.20[c]	0.20[c]
W	0.25[c]	0.25[c]	0.25[c]

V_{accr} (m^3/yr m)	65.82	42.33	41.98
V_{comp} (m^3/yr m)	41.4	27.28	24.65
V_{hydac}(m^3/yr m)	9.8	9.9	7.45

[a] Fluid budget derived from published seismic velocities: line T2933 (EWING9509-2933; McIntosh et al., 2013), L10 (MGL0905-10; Deng et al., 2012) and L27 (MGL0905-27; Lester et al., 2013).

[b] Subduction velocity, corrected for obliquity.

[c] Smectite fraction, water fraction in smectite, values representative for other convergent boundaries (Moore and Vrolijk, 1992; Townend, 1997b; Pecher et al., 2010).

Appendix D. Possible Effects of Thermal Disturbance from Frictional Heating

The analytical solution in Molnar and England (1990) can be used to relate the observed surface heat flux and temperature with shear stress:

$$\mathrm{Q} = \frac{Q_0 + \upsilon\tau}{S} \qquad \text{(D.1)}$$

where Q_0 is the reference heat flow in the region, $\upsilon\tau$ is for frictional heating of the fault with υ the rate of orthogonal plate convergence and τ is the shear stress associated with slip on the fault. S = 1 + b($z_f \upsilon \sin\varphi$ / α), where z_f is depth of the fault below the heat flow measurement, φ is the dip of the fault separating the upper and lower plates, and α is the average thermal diffusivity. We used this analytical solution to calculate the heat flow profile along the Yung-An ridge using the following parameters: ν = 80 (and 40) mm yr^{-1} *cos(50°), with 80 mm yr^{-1} full convergent rate times cosine of the angle between relative plate motion and the strike of the trench axis. Such a high slip rate provides an upper bound. Based on the seismic profile, we used an average dip of 28° to calculate the depth of the fault at different distances from the fault outcrop. We used a diffusivity of 1.1*10^{-6} m^3 yr^{-1} m^{-1} and one for the dimensionless factor b as used by Chi and Reed (2008) for this study area. Shear stresses in the shallow convergent plate boundaries are poorly constrained but mostly estimated between negligible to several tens of megapascal (England, 2018; and references therein).

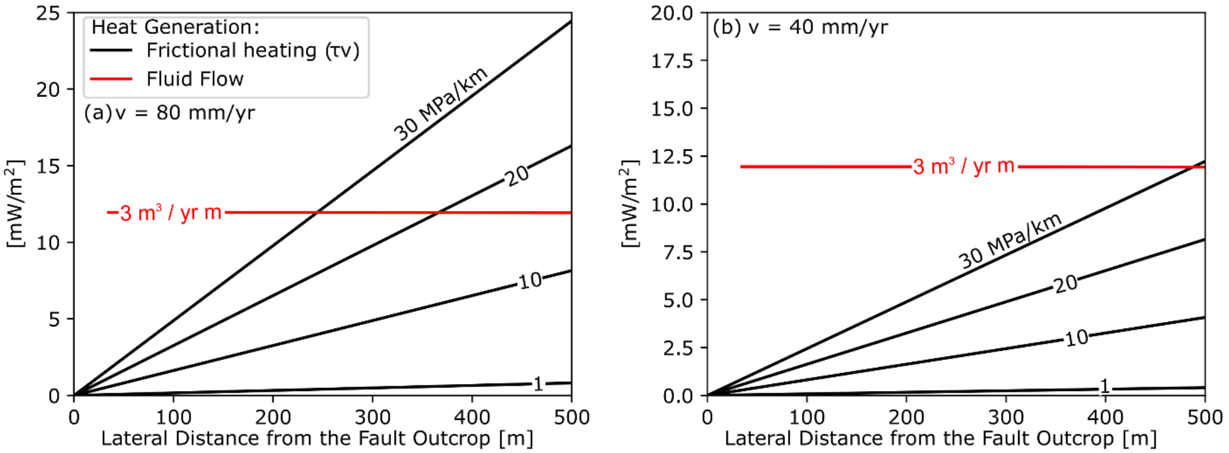

Figure D. 2. A comparison of the magnitude of frictional heat versus heat being advected by fluids along the Yung-An Ridge fault (for location see Figure 1). X-axis depicts the lateral distance from the surface fault outcrop. The frictional heat (black lines) is a product of slip rates υ and shear stress τ, thus proportional to depth through the stress gradient. Its contribution to heat flow over the Yung-An Ridge increases with distance from the fault outcrop, in the order of up to a few tens of mWm^{-2}, assuming stress gradients from 1 to 30 MPa km^{-1} and different slip rates (**a**) υ = 80 mm yr^{-1} and (**b**) 40 mm yr^{-1}. On the contrary, the advective flow contribution to the heat supply (red line; for flow rates of 3 m^3 yr^{-1} m^{-1}) increases towards the seafloor as heat is carried up dip along the fault. The results highlight that the magnitude of frictional heat on the scale of hundreds-of-meters near the fault is small compared to the heat being advected by fluids.

Acknowledgements

We thank IHS for access to Kingdom interpretation software within the academic licensing program. Maps have been drafted using Generic Mapping Tools.

Data availability statement

Information and data from the Expedition EW9509 and MGL0905 are stored at the Marine Geoscience Data System (MGDS) (https://www.marine-geo.org/tools/search/entry.php?id=EW9509 and https://www.marine-geo.org/tools/search/entry.php?id=MGL0905). Seismic data from the Four-Way-Closure Ridge and Yung-An Ridge are available through Berndt et al. (2019) and Kunath et al. (2020) (https://doi.pangaea.de/10.1594/PANGAEA.913192). Data from the Expedition MW9006 can be requested from the Ocean Data Bank website (ODB; http://odb.ntu.edu.tw/seisdb/) or directly by contacting Prof. Char-Shine Liu.

References

Bangs, N. L., McIntosh, K. D., Silver, E. A., Kluesner, J. W., & Ranero, C. R. (2015). Fluid accumulation along the Costa Rica subduction thrust and development of the seismogenic zone. *Journal of Geophysical Research: Solid Earth*, *120*(1), 67-86.

Berndt, C., Chi, W. C., Jegen, M., Lebas, E., Crutchley, G., Muff, et al. (2019). Tectonic controls on gas hydrate distribution off SW Taiwan. *Journal of Geophysical Research: Solid Earth*, *124*(2), 1164-1184.

Brown, K. M., Tryon, M. D., DeShon, H. R., Dorman, L. M., & Schwartz, S. Y. (2005). Correlated transient fluid pulsing and seismic tremor in the Costa Rica subduction zone. *Earth and Planetary Science Letters*, *238*(1-2), 189-203.

Carson, B., Holmes, M. L., Umstattd, K., Strasser, J. C., & Johnson, H. P. (1991). Fluid expulsion from the Cascadia accretionary prism: evidence from porosity distribution, direct measurements, and GLORIA imagery. *Phil. Trans. R. Soc. Lond. A*, *335*(1638), 331-340.

Carson, B., & Screaton, E. J. (1998). Fluid flow in accretionary prisms: Evidence for focused, time- variable discharge. *Reviews of Geophysics*, *36*(3), 329-351.

Chen, L., Chi, W. C., Wu, S. K., Liu, C. S., Shyu, C. T., Wang, Y., & Lu, C. Y. (2014). Two dimensional fluid flow models at two gas hydrate sites offshore southwestern Taiwan. *Journal of Asian Earth Sciences*, *92*, 245-253.

Chi, W. C., Reed, D. L., Liu, C. S., & Lundberg, N. (1998). Distribution of the bottom-simulating reflector in the offshore Taiwan collision zone. *Terr. Atmos. Ocean. Sci*, *9*(4), 779-794.

Chi, W. C., & Reed, D. L. (2008). Evolution of shallow, crustal thermal structure from subduction to collision: An example from Taiwan. *Geological Society of America Bulletin*, *120*(5-6), 679-690.

Chuang, P. C., Yang, T. F., Hong, W. L., Lin, S., Sun, C. H., Lin, A. S., et al. (2010). Estimation of methane flux offshore SW Taiwan and the influence of tectonics on gas hydrate accumulation. *Geofluids, 10*(4), 497-510.

Davis, E. E., Becker, K., Pettigrew, T., Carson, B., & MacDonald, R. (1992). CORK: a hydrologic seal and downhole observatory for deep-ocean boreholes. In *Davis, EE, Mottl, MJ, Fisher, AT, et al., Proc. ODP, Init. Repts* (Vol. 139, pp. 43-53).

Davis, E. E., Becker, K., Wang, K., Carson, B. (1995). Long-term observations of pressure and temperature in Hole 892B, Cascadia accretionary prism. In *Proc. ODP, Scientific Results* (Vol. 146, No. 1, pp. 299-311).

Davis, E. E., Becker, K., Wang, K., Obara, K., Ito, Y., & Kinoshita, M. (2006). A discrete episode of seismic and aseismic deformation of the Nankai trough subduction zone accretionary prism and incoming Philippine Sea plate. *Earth and Planetary Science Letters*, *242*(1-2), 73-84.

Davis, E. E., & Villinger, H. W. (2006). Transient formation fluid pressures and temperatures in the Costa Rica forearc prism and subducting oceanic basement: CORK monitoring at ODP Sites 1253 and 1255. *Earth and Planetary Science Letters*, *245*(1-2), 232-244.

Deng, J. M., Wang, T. K., Yang, B. J., Lee, C. S., Liu, C. S., & Chen, S. C. (2012). Crustal velocity structure off SW Taiwan in the northernmost South China Sea imaged from TAIGER OBS and MCS data. *Marine Geophysical Research*, *33*(4), 327-349.

Ellis, S., Fagereng, Å., Barker, D., Henrys, S., Saffer, D., Wallace, L., et al. (2015). Fluid budgets along the northern Hikurangi subduction margin, New Zealand: The effect of a subducting seamount on fluid pressure. *Geophysical Journal International*, *202*(1), 277-297.

England, P. (2018). On shear stresses, temperatures, and the maximum magnitudes of earthquakes at convergent plate boundaries. *Journal of Geophysical Research: Solid Earth*, *123*(8), 7165-7202.

Fisher, A. T., & Hounslow, M. W. (1990). Transient fluid flow through the toe of the Barbados accretionary complex: constraints from ocean drilling program leg 110 heat row studies and simple models. *Journal of Geophysical Research: Solid Earth*, *95*(B6), 8845-8858.

Fulton, P. M., Brodsky, E. E., Kano, Y., Mori, J., Chester, F., Ishikawa, T., et al. (2013). Low coseismic friction on the Tohoku-Oki fault determined from temperature measurements. *Science*, *342*(6163), 1214-1217.

Fulton, P. M., Harris, R. N., Saffer, D. M., & Brodsky, E. E. (2010). Does hydrologic circulation mask frictional heat on faults after large earthquakes?. *Journal of Geophysical Research: Solid Earth*, *115*(B9).

Grevemeyer, I., & Villinger, H. (2001). Gas hydrate stability and the assessment of heat flow through continental margins. *Geophysical Journal International*, *145*(3), 647-660.

Hamilton, E. L. (1980). Geoacoustic modeling of the sea floor. *The Journal of the Acoustical Society of America*, *68*(5), 1313-1340.

Hensen, C., Wallmann, K., Schmidt, M., Ranero, C. R., & Suess, E. (2004). Fluid expulsion related to mud extrusion off Costa Rica—a window to the subducting slab. *Geology*, *32*(3), 201-204.

Hornbach, M. J., Saffer, D. M., Holbrook, W. S., Van Avendonk, H. J., & Gorman, A. R. (2008). Three- dimensional seismic imaging of the Blake Ridge methane hydrate province: Evidence for large, concentrated zones of gas hydrate and morphologically driven advection. *Journal of Geophysical Research: Solid Earth*, *113*(B7).

Von Huene, R., Klaeschen, D., Gutscher, M., & Fruehn, J. (1998). Mass and fluid flux during accretion at the Alaskan margin. *Geological Society of America Bulletin*, *110*(4), 468-482.

Jaeger, J. C., & Carslaw, H. S. (1959). *Conduction of heat in solids*. Clarendon P.

Kunath, P., Chi, W. C., Berndt, C., Chen, L., Liu, C. S., Kläschen, D., & Muff, S. (2020). A shallow seabed dynamic gas hydrate system off SW Taiwan: Results from 3- D seismic, thermal, and fluid migration analyses. *Journal of Geophysical Research: Solid Earth*, *125*(11), e2019JB019245-T.

Lauer, R. M., & Saffer, D. M. (2012). Fluid budgets of subduction zone forearcs: the contribution of splay faults. *Geophysical Research Letters*, *39*(13).

Lester, R., McIntosh, K., Van Avendonk, H. J., Lavier, L., Liu, C. S., & Wang, T. K. (2013). Crustal accretion in the Manila trench accretionary wedge at the transition from subduction to mountain-building in Taiwan. *Earth and Planetary Science Letters*, *375*, 430-440.

Lin, A. T., Yao, B., Hsu, S. K., Liu, C. S., & Huang, C. Y. (2009). Tectonic features of the incipient arc-continent collision zone of Taiwan: Implications for seismicity. *Tectonophysics*, *479*(1-2), 28-42.

Linke, P., Suess, E., Torres, M., Martens, V., Rugh, W. D., Ziebis, W., & Kulm, L. D. (1994). In situ measurement of fluid flow from cold seeps at active continental margins. *Deep Sea Research Part I: Oceanographic Research Papers*, *41*(4), 721-739.

Liu, C.-S., P. Schnürle, Y. Wang, S.H. Chung, S.C. Chen, and T.H. Hsiuan (2006) Distribution and characters of gas hydrate offshore southwestern Taiwan. Terrestrial, Atmospheric and Oceanic Sciences, 17(4), 615-644.

Mann, D., & Kukowski, N. (1999). Numerical modelling of focused fluid flow in the Cascadia accretionary wedge. *Journal of Geodynamics*, *27*(3), 359-372.

McIntosh, K., van Avendonk, H., Lavier, L., Lester, W. R., Eakin, D., Wu, F., et al. (2013). Inversion of a hyper-extended rifted margin in the southern Central Range of Taiwan. *Geology*, *41*(8), 871-874.

Minshull, T., & White, R. (1989). Sediment compaction and fluid migration in the Makran accretionary prism. *Journal of Geophysical Research: Solid Earth*, *94*(B6), 7387-7402.

Molnar, P., & England, P. (1990). Temperatures, heat flux, and frictional stress near major thrust faults. *Journal of Geophysical Research: Solid Earth*, *95*(B4), 4833-4856.

Moore, J. C., Klaus, A., Bangs, N. L., Bekins, B., Bücker, C. J., Brückmann, W., et al. (1998). Consolidation patterns during initiation and evolution of a plate-boundary decollement zone: Northern Barbados accretionary prism. *Geology*, *26*(9), 811-814.

Moore, J. C., & Vrolijk, P. (1992). Fluids in accretionary prisms. *Reviews of Geophysics*, *30*(2), 113-135.

Ministry of Science and Technology (MOST). (2018, June 25). First recovery of hydrate offshore SW Taiwan (in Chinese). Retrieved from https://www.most.gov.tw/folksonomy/ detail?subSite=&l=ch&article _uid=34170631-2eef-4af5-b15d-b0eb725b9974&menu_id =9aa56881-8df0-4eb6 a5a7-32a2f72826ff&content_type=P&view_mode=list . View as on April 29, 2019.

Pecher, I. A., Henrys, S. A., Wood, W. T., Kukowski, N., Crutchley, G. J., Fohrmann, M., et al. (2010). Focussed fluid flow on the Hikurangi Margin, New Zealand—Evidence from possible local upwarping of the base of gas hydrate stability. *Marine Geology*, *272*(1-4), 99-113.

Ranero, C. R., Grevemeyer, I., Sahling, H., Barckhausen, U., Hensen, C., Wallmann, K., et al.(2008). Hydrogeological system of erosional convergent margins and its influence on tectonics and interplate seismogenesis. *Geochemistry, Geophysics, Geosystems*, *9*(3).

Reed, D. and C. Liu, (2014). Raw Multi-Channel Seismic Shot Data from the Western Philippine Sea acquired during R/V Maurice Ewing expedition EW9509 (1995). Interdisciplinary Earth Data Alliance (IEDA). doi:10.1594/IEDA/309962.

Saffer, D. M., & Tobin, H. J. (2011). Hydrogeology and mechanics of subduction zone forearcs: Fluid flow and pore pressure. *Annual Review of Earth and Planetary Sciences*, *39*, 157-186.

Schnürle, P., Liu, C. S., Lin, A. T., & Lin, S. (2011). Structural controls on the formation of BSR over a diapiric anticline from a dense MCS survey offshore southwestern Taiwan. *Marine and petroleum geology*, *28*(10), 1932-1942.

Screaton, E. J., Carson, B., & Lennon, G. P. (1995). Hydrogeologic properties of a thrust fault within the Oregon accretionary prism. *Journal of Geophysical Research: Solid Earth*, *100*(B10), 20025-20035.

Shipley, T. H., Houston, M. H., Buffler, R. T., Shaub, F. J., McMillen, K. J., Ladd, J. W., & Worzel, J. L. (1979). Seismic evidence for widespread possible gas hydrate horizons on continental slopes and rises. *AAPG bulletin*, *63*(12), 2204-2213.

Shipley, T. H., Moore, G. F., Tobin, H. J., & Moore, J. C. (1997). Synthesis of the Barbados décollement seismic reflection response from drilling-based geophysical observations and physical properties. In *Proceedings of the Ocean Drilling Program. Scientific results* (Vol. 156, pp. 293-302).

Shyu, C. T., Yu-Jhong, C., Chiang, S. T., & Liu, C. S. (2006). Heat flow measurements over bottom simulating reflectors, offshore southwestern Taiwan. *TAO: Terrestrial, Atmospheric and Oceanic Sciences*, *17*(4), 845

Solomon, E. A., Kastner, M., Wheat, C. G., Jannasch, H., Robertson, G., Davis, E. E., & Morris, J. D. (2009). Long-term hydrogeochemical records in the oceanic basement and forearc prism at the Costa Rica subduction zone. *Earth and Planetary Science Letters*, *282*(1-4), 240-251.

Suppe, J. (1984). Kinematics of arc-continent collision, flipping of subduction and back-arc spreading near Taiwan: Memoir of the Geological Society of China, 21-33.

Teng, L. S. (1990). Geotectonic evolution of late Cenozoic arc-continent collision in Taiwan. *Tectonophysics*, *183*(1-4), 57-76.

Tinivella, U., & Giustiniani, M. (2013). Variations in BSR depth due to gas hydrate stability versus pore pressure. *Global and Planetary Change*, *100*, 119-128.

Townend, J. (1997). Subducting a sponge: minimum estimates of the fluid budget of the Hikurangi Margin accretionary prism. *Geological Society of New Zealand Newsletter*, *112*, 14-16.

Vasseur, G., Demongodin, L., & Bonneville, A. (1993). Thermal Modelling of Fluid Flow Effects in Thin- Dipping Aquifers. *Geophysical Journal International*, *112*(2), 276-289.

Villinger, H. W., Tréhu, A. M., & Grevemeyer, I. (2010). Seafloor marine heat flux measurements and estimation of heat flux from seismic observations of bottom simulating reflectors. *Geophysical characterization of gas hydrates*, 279-300.

Westbrook, G. K., et al., (1994). *Proceedings of the Ocean Drilling Program Initial Report, vol. 146, Ocean Drill. Program, College Station, Tex.*

Yamano, M., Foucher, J. P., Kinoshita, M., Fisher, A., Hyndman, R. D., Leg, O. D. P., & Party, S. S. (1992). Heat flow and fluid flow regime in the western Nankai accretionary prism. *Earth and Planetary Science Letters*, *109*(3-4), 451-462.

Zwart, G., Moore, J. C., & Cochrane, G. R. (1996). Variations in temperature gradients identify active faults in the Oregon accretionary prism. *Earth and Planetary Science Letters*, *139*(3-4), 485-495.

Figures and Tables Captions

Figure 1. Bathymetry map of the area offshore SW Taiwan. The South China Sea plate (SCS) subducts under the Philippine Sea Plate (PSP) at a rate of 7-9 cm yr^{-1} (black arrow indicates relative motion), forming the Taiwan accretionary prism. Red lines show the multi-channel seismic (MCS) tracks used in this study to quantify the regional geothermal gradients. Of these tracks, we calculate the fluid budget along three transects in the north and south portion of the prism: T2933 (EW9509-2933, McIntosh et al., 2013), L10 (MGL0905-10, Deng et al., 2012) and L27 (MGL0905-27, Lester et al., 2013). We present the seismic profiles of the Four-Way-Closure Ridge (FWCR; Figure 7), Yung-An Ridge (YAR; Figure 6) and EW9509-33 (EW; Figure 5) transects as examples of the analysis we performed on all MCS lines; the other seismic profiles have been previously published (Liu et al., 1997; Chi et al., 1998; Chi & Reed, 2008).

Figure 2. **a.** Schematic of the physical model. Thin permeable dipping structure of constant thickness (a) cross-cuts a homogeneous impermeable medium. The flow of high temperature fluids along the conduit causes thermal anomalies in the hanging and footwall expressed as deviations from the purely conductive thermal model. **b.** Lateral isotherms resulting from localized fluid flow at various values of Pe tan(φ). Higher values of Pe tanφ lead to greater thermal disturbances that reach further towards the seafloor. **c.** Steady-state normalized temperature disturbance (ΔT') as a function of the normalized horizontal distance (x'; modified from Vasseur et al., 1993). x'= 0 and x' = 1 represent the horizontal location for the origin of fluid advection and the discharge area, respectively. Note in c, the conduit is dipping to the left.

Figure 3. Geothermal modelling at ODP Site 892. **a.** Sketch of Site 892 seismic profile (modified after Mann and Kukowski, 1999). Borehole crosscuts the BSR and interpreted fault

(black line). Seafloor temperature, geothermal gradient, and thermal conductivity were taken from Westbrook et al. (1994) and Zwart et al. (1996). **b.** Temperature misfit between predicted and observed temperature along the BSR at a range of source depths and flow rates. The red star marks the minimum misfit, which is our preferred model. The red line around the minimum shows the contour of constant misfit, equal to 0.4°C. **c.** Modeled conductive-only 2D temperature field. **d.** Modeled 2D temperature field including fluid advection with the optimized parameters. Note the higher temperature along the fault due to the fluid flow. Small circles in c and d indicate the observed BSR location and their color the BSR derived temperatures.

Figure 4. Shaded relief offshore SW Taiwan with geothermal gradient and fluid flow rate information overlaid. Geothermal gradients are calculated across the region from BSR depths in previously collected MCS profiles (Figure 1). Stars (Chi & Reed, 2008) and inverted triangles indicate geothermal gradients calculated from the observed BSR depth, while pentagons indicates gradients determined from thermal probe measurements (Shyu et al., 2006). Flow rates are calculated at a number of sites in the region where either faults (circle) or the base of a slope basin (diamonds) act as the conduit. Black dotted boxes indicate areas where regional average flow rate are calculated. Red lines denote position of seismic transects Deng et al. (2012), McIntosh et al. (2013) and Lester et al. (2013) referred to in this paper.

Figure 5. **a.** Seismic profile in the northern section of the accretionary prism (Figures 1 and 4; Line EW). Red and green lines mark interpreted BSR and fault locations, respectively. **b.** A comparison of the BSR-derived (black lines) and 2D steady-state conductive-only modeled (blue lines) geothermal gradients along Line EW. At Ridge 1, localized, laterally varying temperature gradient on either side of the fault suggests active fluid flow within the fault. In contrast, at Ridges 2 and 3, agreement between the modeled geothermal gradients suggests that topography

is the controlling factor. We derive the BSR subbottom depth and the fault geometry using the empirical Hamilton equation (Hamilton, 1980).

Figure 6. **a**. Seismic profile across the Yung-An Ridge (for location see Fig 1). There is a clear discrepancy (marked with red arrows) between the observed BSR (black) and the theoretical conduction only BSR (blue). **b.** Absolute temperature discrepancy at BSR depth between our preferred model and the observed BSR. d' is the lateral extent in the hanging wall part, as shown in Fig 6a. **c.** Geothermal gradients across the profile, theoretical 2D steady state conductive only temperature gradient (blue), BSR derived temperature gradient (black), and temperature gradient derived by our geothermal model (red) that considers fluid flow. **d.** Grid of misfit values between predicted and observed temperature along the BSR.

Figure 7 a. Seismic profile across the Four-Way-Closure Ridge (for location see Fig 1). There is a clear discrepancy (marked with red arrows) between the observed BSR (black) and the theoretical conduction only BSR (blue). Heat flow measurements have been acquired during SONNE266 (Bohrmann et al., 2018). d' marks the lateral extent within the slope basin strata, as shown in Fig 7a. **b.** Absolute temperature discrepancy at BSR depth between our preferred model and the observed BSR. **c.** Geothermal gradients across the profile, theoretical 2D steady state conductive only temperature gradient (blue), BSR derived temperature gradient (black), and temperature gradient derived by our geothermal model (red). **d.** Grid of misfit values between predicted and observed temperature along the BSR. Black lines show the regions of constant misfit equal to 2 and 3 ^{o}C.

Figure 8. **a.** Conceptual model of fluid cycle in an accretionary wedge. Fluid sources include pore fluid in incoming sediments (a) and fluid released from illite-smectite transition deeper in

the wedge. Fluid sinks (c) include focused discharge (c_1) and expulsion via diffusion, compaction, or other physical processes (c_2). **b-d.** Interpreted seismic profiles and fluid flow rate calculations of northern lines, EW9509-T2933 (McIntosh et al., 2013) and MGL0905-10 (Deng et al., 2012), and southern line, MGL0905-27 (Lester et al., 2013). Each seismic profile shows the seafloor (black lines), observed BSR locations (red lines), and interpreted faults (solid green lines) and slope basin boundaries (dashed green lines). We derive the BSR subbottom depth and the fault geometry using the empirical Hamilton equation (Hamilton, 1980). Numbers in boxes indicate local flow rates in m^3 yr^{-1} m^{-1}. See Figure 4 for transect locations and areas where regional discharge rates are calculated (Figure 4; black dashed lines).

Figure 9. Theoretical cooling effect due to thrusting along Yung-An Ridge seismic profile off SW Taiwan (for location see Fig 1). **a.** and **b.** A comparison of the BSR-derived (dashed-dotted line), 2D steady-state conductive-only modeled (densely dashed line) and derived from the analytical solution from Molnar and England (1990) (black lines) geothermal gradients. The stress gradients from 1 to 30 MPa km^{-1} and different slip rates (a. v = 80 mm yr^{-1} (Fig. 9a) and 40 mm yr^{-1} (Fig. 9b)). X-axis depicts the lateral distance from the surface fault outcrop. d' marks the lateral extent in the hanging wall part, as shown in Fig 6a. The temperature gradients decrease due to under thrusting of the cold footwall block near the fault trace, except for larger stress gradients (i.e., 30MPa km^{-1}), and then increase due to the frictional heating related to the stress gradient. The clear discrepancies between the geothermal gradients derived from the analytical solution from Molnar and England and the BSR suggest that frictional heating is not a controlling factor for the localized temperature anomalies near the fault. By using a slower slip rates (< 40 mm yr^{-1}), the fit will be even worse.

Table 1. Fluid sources, sinks, and reservoirs for two northern transects in the initial collision zone and one southern transects in the in the subduction zone of the Taiwan accretionary prism.

Table 1. Fluid sources, sinks, and reservoirs for two northern transects in the initial collision zone and one southern transects in the in the subduction zone of the Taiwan accretionary prism.

	a	b	c	c_1	c_2	d	e	e_1
	V_{accr}	V_{hydac}	V_{comp}	Focused Discharge	Diffusive Flow and others	Remaining Fluids	$\frac{\text{Focused Flow}}{\text{Diffusive Flow}}$	$\frac{\text{Focused Flow}}{V_{comp}}$
	(m^3/yr m)	(m^3/yr m)	(m^3/yr m)	(m^3/yr m)	(m^3/yr m)	(m^3/yr m)		
Northern Transects								
T2933	65.82	9.8	41.4	19.55	21.85	34.22	0.98	0.47
L10	42.33	9.9	27.28	8.25	19.03	24.95	0.43	0.30
Southern Transect								
L27	41.98	7.45	24.65	6.5	18.15	24.78	0.34	0.26

[*] Large offset seismic transects T2933 (EWING9509-2933; McIntosh et al., 2013), L10 (MGL0905-10; Deng et al., 2012) and L27 (MGL0905-27; Lester et al., 2013).